Chapter 2
Laser Schlieren and Shadowgraph

Keywords Knife-edge · Gray-scale filter · Cross-correlation · Background oriented schlieren.

2.1 Introduction

Schlieren and shadowgraph techniques are introduced in the present chapter. Topics including optical arrangement, principle of operation, and data analysis are discussed. Being refractive index-based techniques, schlieren and shadowgraph are to be compared with interferometry, discussed in Chap. 1. Interferometry assumes the passage of the light beam through the test section to be straight and measurement is based on phase difference, created by the density field, between the test beam and the reference beam. Beam bending owing to refraction is neglected in interferometry and is a source of error. Schlieren and shadowgraph dispense with the reference beam, simplifying the measurement process. They exploit refraction effects of the light beam in the test section. Schlieren image analysis is based on beam deflection (but not displacement) while shadowgraph accounts for beam deflection as well as displacement [3, 8, 10]. In its original form, shadowgraph traces the path of the light beam through the test section and can be considered the most general approach among the three. Quantitative analysis of shadowgraph images can be tedious and, in this respect, schlieren has emerged as the most popular refractive index-based technique, combining ease of instrumentation with simplicity of analysis.

P. K. Panigrahi and K. Muralidhar, *Schlieren and Shadowgraph Methods in Heat and Mass Transfer*, SpringerBriefs in Thermal Engineering and Applied Science,
DOI: 10.1007/978-1-4614-4535-7_2,

2.2 Laser Schlieren

A basic schlieren setup using concave mirrors that form the letter Z is shown in Fig. 2.1. The Z-type monochrome schlieren system comprises concave mirrors, flat mirrors, a knife-edge, and a laser as a light source. The optical components and the lasers are kept on a common centerline at a certain elevation. Under undisturbed conditions, the original laser beam as well as the center of the collimated beam (after expansion and collimation) fall on the central portion of the optical components. For the images presented in the following chapters, concave mirrors of the schlieren apparatus are of 1.3 m focal length each and 200 mm diameter. Relatively large focal lengths of the concave mirrors make the schlieren technique quite sensitive to the thermal/concentration gradients. Out of the two concave mirrors, the first acts as the collimator while the second concave mirror placed after the test cell decollimates the laser beam with a focus at a knife-edge. Flat mirror M1 directs the diverging laser beam onto the first concave mirror which collimates it into a beam of uniform diameter. The collimated beam passes through the test section and falls on the second concave mirror which focuses it onto the plane of the knife-edge. The test section is placed between the two concave mirrors. Optical elements are supported on adjustable mounts (with permissible movements in x and y directions, z being the direction of propagation of the laser beam). Slight misalignment in the system with respect to the direction of the laser beam can be taken care of by adjusting the mounts. The knife-edge is placed at the focal plane of the second concave mirror. It is positioned to cutoff a part of the light focused on it, so that in the absence of any disturbance in the test section, the illumination on the screen is uniformly reduced. The mount holding the knife-edge ensures that the knife-edge has flexibility in orientation, say, vertical or horizontal as required in the measurement being carried out. The mount permits the movement of the knife-edge parallel to the direction of the laser beam as well as in plane, so as to cutoff the desired extent of light intensity. In practice, the knife-edge is set perpendicular to the direction in which the density gradients are to be observed. In many applications discussed in the present monograph, density gradients are predominantly in the vertical direction and the knife-edge has been kept horizontal. The initial light intensity values (on a gray scale of 0–255) have been chosen to be <20, making the image look uniformly dark.

Schlieren measurements rely on intensity of light measured in turn by the CCD camera. Within limits, the sensor array of the camera is a linear device and converts intensity to voltage in direct proportion. Beyond the range, nonlinearities set in and the camera is said to be saturated. Since the light falling at the knife-edge is a spot, light intensities are large, and a neutral density filter may be used to uniformly reduce illumination reaching the camera. The screen shown in Fig. 2.1 serves this purpose as well. There could, however, be a disadvantage of non-uniformities of the screen creating errors in intensity measurement and should be addressed. Alternatively, an additional lens can collimate the spot formed at the knife-edge and create a light beam of larger diameter and lower intensity for the camera.

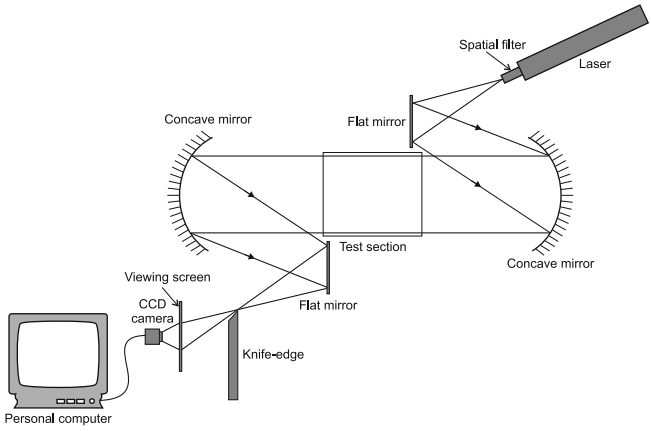

Fig. 2.1 Schematic diagram of a *Z*-type laser schlieren setup

The issue of camera saturation is serious when lasers are used as a light source. White light sources may also be used in the context of schlieren since coherence is not a matter of concern here. The light source, in the present monograph is, however, a laser, except for discussions related to Chap. 3.

2.2.1 Positioning the Knife-Edge

Before the start of experiments, the schlieren setup (Fig. 2.1) has to be carefully aligned. Apart from issues, such as collimation, focus, and uniform light intensity over the collimated light beam, the adjustment of the knife-edge plays a significant role in the quality of the schlieren image recorded. With best alignment, the undisturbed light beam should form a spot at the knife-edge whose dimensions match the diameter of the pinhole used in the spatial filter (except for scaling introduced by the focal lengths of the optical elements). As the knife-edge is moved to block the spot of light, the intensity of illumination decreases uniformly over the screen. This effect is demonstrated in Fig. 2.2 where the distribution of light intensity over the screen is shown for various positions of the knife-edge. Figure 2.2a and c respectively show non-uniform distribution of light intensity when the knife-edge is either too close or too far away from the second concave mirror. Figure 2.2b shows light intensity distribution for a correctly placed knife-edge partly blocking the light spot. An important step in the alignment procedure is to adjust the percent cutoff by the knife-edge in order to obtain the desired sensitivity. If the cutoff is small, a large amount of light passes over to the screen and results in poor contrast of the schlieren images along with the possibility of camera saturation. If the cutoff is large, high contrast images are possible but the measurement may result in the loss of information in regions of low density gradient.

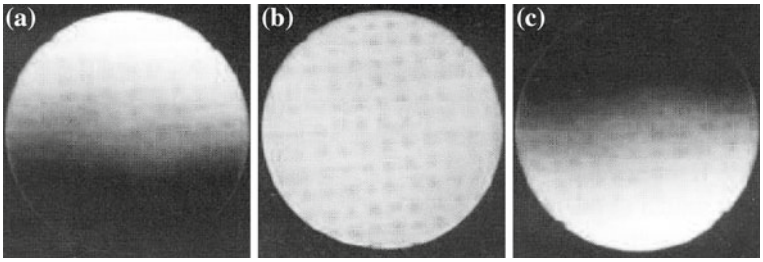

Fig. 2.2 Effect of knife-edge movement on the schlieren image for a horizontal knife-edge cutting off the light beam from below. **a** Knife-edge is very close to the second concave mirror; **b** Knife-edge is correctly placed. **c** Knife-edge is beyond the focal plane of the second concave mirror [8]

Disturbances to a schlieren system include floor vibrations, heavy machinery, and also the movement of laboratory personnel in the vicinity. The schlieren technique, however, is not nearly as vibration-sensitive as interferometry, where motion amplitudes of the order of a light wavelength are visible in the form of fringes. Since schlieren depends primarily on geometric, rather than principles of wave-optics, it is superior to interferometry in its resistance to shock and vibrations. If the sensitivity of the schlieren system is deliberately reduced, either by a lower intensity cutoff by the knife-edge, or by replacing the knife-edge with a graded (gray-scale) filter, vibration errors would be truly minimal.

2.2.2 Analysis of Schlieren Images

The present section analyzes the process of image formation in a schlieren setup. The index of refraction (or its spatial derivatives) determines the resulting light intensity pattern over the screen. An aspect shared by interferometry and schlieren (and indeed, shadowgraph) is that they generate projection data, namely information integrated in the direction of propagation of the light beam. The result is a concentration (or temperature) field that is ray-averaged, specifically, integrated over the length L of the test section [9].

As discussed in Chap. 1, refractive index techniques depend on the unique refractive index—density relationship for transparent media. Called the Lorentz–Lorenz formula, it is expressed as:

$$\frac{n^2 - 1}{\rho(n^2 + 2)} = \text{constant} \tag{2.1}$$

where n is refractive index and ρ, the density. For gases, the refractive index is close to unity and the expression reduces to the Gladstone–Dale equation

$$\frac{n-1}{\rho} = \text{constant} \tag{2.2}$$

For a given wavelength, the constant appearing in Eqs. 2.1 and 2.2 can be evaluated from the knowledge of n and ρ under reference conditions. It depends on the chemical composition of the material and varies slightly with wavelength. In general, density of pure fluids will depend on pressure and temperature. In many applications involving gases, pressure is sensibly constant and density scales entirely with temperature. Liquids such as water are practically incompressible and their density will vary only with temperature. Within limits, this variation of density with temperature can be taken to be linear. Hence, refractive index will itself scale linearly with temperature. For a process involving mass transfer, the Lorentz–Lorenz formula as applied to a solute–solvent system takes the form:

$$\frac{n^2-1}{n^2+2} = \frac{4}{3}\pi(\alpha_A N_A + \alpha_B N_B) \tag{2.3}$$

Here n is the refractive index of the solution, and α and N are respectively the polarizability and mole fraction. This result is often used in crystal growth applications with suffixes A and B specifying water as the solvent and KDP as the solute, respectively [4–6]. The material property that determines the sensitivity of the optical measurement is $\mathrm{d}n/\mathrm{d}T$ (or $\mathrm{d}n/\mathrm{d}C$). Compared to gases, the derivative is about three orders of magnitude larger in liquids. Hence, only a small perturbation is needed to see refraction in liquids compared to air.

Image formation in a schlieren system arises from the deflection of the light beam in a variable refractive index field toward a region of higher refractive index. In order to recover quantitative information from a schlieren image, one has to determine the cumulative angle of refraction of the light beam emerging from the test cell as a function of position in the cross-sectional $x - y$ plane [3]. This plane is normal to the light beam, whose direction of propagation is along the z-direction. The path of the light beam in a medium whose index of refraction varies in the vertical direction (y) can be analyzed using the principles of geometric optics as follows (also see Sect. 1.4.5):

Consider two wavefronts at times τ and $\tau + \Delta\tau$, separated by a small time difference $\Delta\tau$, Fig. 2.3. At time τ the ray is at a position z. After a interval $\Delta\tau$, the light has moved a distance of $\Delta\tau$ times the speed of light c. Since c depends on refractive index, it is a function of y. In addition, the wavefront turns through an angle $\Delta\alpha$. The local speed of light is c_0/n where c_0 is the velocity of light in vacuum and n is the local refractive index of the medium. Hence the distance Δz that the light beam travels during time interval $\Delta\tau$ is

$$\Delta z = \Delta\tau \frac{c_0}{n}$$

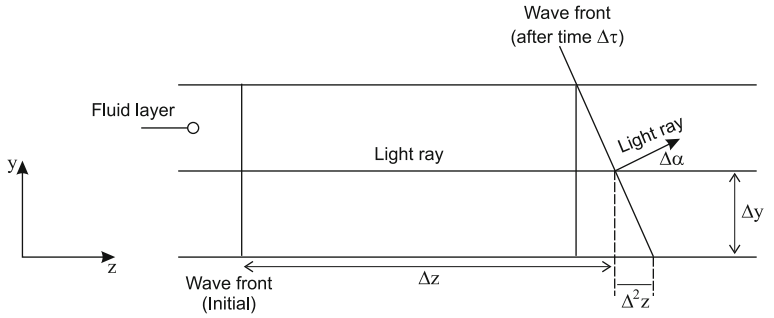

Fig. 2.3 Bending of a light ray in a vertically stratified fluid medium due to refraction

The gradient in refractive index along the y direction results in bending of the wavefront. Let $\Delta\alpha$ represent the bending angle at a location z. A small increment $\Delta\alpha$ in angle α can be expressed as

$$\Delta\alpha \approx \tan(\Delta\alpha) = \frac{\Delta^2 z}{\Delta y}$$

The distance $\Delta^2 z$ is given by

$$\Delta^2 z = \Delta z_y - \Delta z_{y+\Delta y} \approx \Delta z_y - \Delta z_y - \frac{\Delta}{\Delta y}(\Delta z)(\Delta y) = -c_0 \frac{\Delta(1/n)}{\Delta y}\Delta\tau\,\Delta y$$

Hence

$$\Delta\alpha = \frac{\Delta^2 z}{\Delta y} = -c_0 \frac{\Delta(1/n)}{\Delta y}\Delta\tau = -n\Delta z \frac{\Delta(1/n)}{\Delta y}$$

In the limiting case

$$d\alpha = \frac{1}{n}\frac{\partial n}{\partial y}\mathrm{d}z = \frac{\partial(\ln n)}{\partial y}\mathrm{d}z \tag{2.4}$$

Hence, the cumulative angle through which the light beam has turned over the length L of the test region is

$$\alpha = \int_0^L \frac{\partial(\ln n)}{\partial y}\mathrm{d}z \tag{2.5}$$

where the integration is performed over the entire length of the test section. It is to be understood that the angle α is a function of the coordinates x and y on the exit plane of the test cell. If the index of refraction within the test section is different from that of the ambient air (n_a), angle α'' of the light beam emerging from the test cell is given by Snell's law

$$n_a \sin\alpha'' = n \sin\alpha$$

Assuming α and α'' to be small angles, we get

$$\alpha'' = \frac{n}{n_a}\alpha$$

Therefore, from Eq. 2.5, we get

$$\alpha'' = \frac{n}{n_a}\int_0^L \frac{1}{n}\frac{\partial n}{\partial y}\mathrm{d}z$$

If the factor $1/n$ within the integrand does not change greatly through the test section, then

$$\alpha'' = \frac{1}{n_a}\int_0^L \frac{\partial n}{\partial y}\mathrm{d}z$$

Since $n_a \approx 1.0$ the cumulative angle of refraction of the light beam emerging into the surrounding air is given by

$$\alpha'' = \int_0^L \frac{\partial n}{\partial y}\mathrm{d}z \tag{2.6}$$

A schlieren system can be thought of as a device to measure the angle α. In most applications, this angle is quite small, say, of the order of 10^{-6}-10^{-3} radians. It is then reasonable to expect that refractive index gradients lead to the light beam getting displaced in the plane of the knife-e.g., out-of-plane effects being negligible in comparison. The small angle approximation helps in image analysis and is uniformly used through out in the following discussion.

Consider the schlieren measurement system shown in Fig. 2.4 comprising lenses instead of concave mirrors. A light source that generates a light beam of diameter a_s is kept at the focus of lens L_1. Thus, a parallel beam of light is created that probes the density distribution in the test section. The dotted line shows the path of the light beam in the presence of disturbance in the test region. The second lens L_2, whose focus is the knife-edge collects the light beam and passes onto a screen. As discussed by Goldstein [3], the screen is ideally located at the conjugate focus of the test section. This position ensures that intensity changes are related to beam deflection alone, as required in schlieren, and not beam displacement (the *shadowgraph* effect). If no disturbance is present, the passage of the light beam is shown by solid lines reaching the focus of L_2, Fig. 2.5, with diameter a_0. This dimension is related to the initial as

$$\frac{a_0}{a_s} = \frac{f_2}{f_1}$$

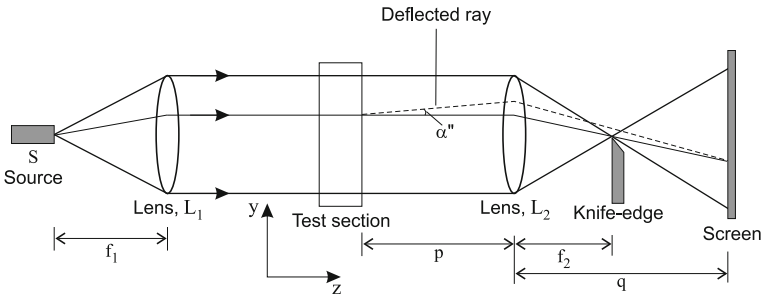

Fig. 2.4 Schematic drawing that shows the path of the light beam in a schlieren system made of lenses. When the screen is at the conjugate focus, the relationship $(1/p)+(1/q) = (1/f_2)$ is followed and the image on the screen is the same size as the cross-section of the test section corresponding to the location p. For the distances shown, the angle detected at the screen is the cumulative turning of the light beam within the test cell. Figure redrawn from [3]

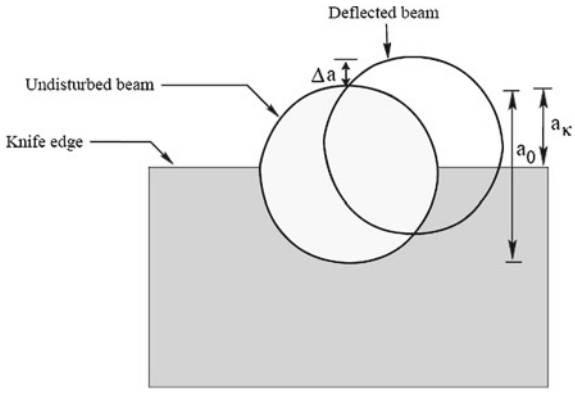

Fig. 2.5 View of undisturbed and deflected light beam cross-sections at the knife-edge of a schlieren system. The horizontal displacement of the light beam does not contribute to intensity contrast

where f_1 and f_2 are the focal lengths of lenses L_1 and L_2, respectively. In a schlieren system, the knife-edge kept at the focal length of the second convex lens is first adjusted, when no disturbance in the test region is present, to cutoff all but an amount corresponding to the dimension a_k of the light beam. Let a_0 be the original size of the laser beam falling on the knife-edge. If the knife-edge is properly positioned, the illumination at the screen changes uniformly, depending upon its direction of the movement. Let I_0 be the illumination at the screen when no knife-edge is present. The illumination I_k with the knife-edge inserted in the focal plane of the second lens but without any disturbance in the test region will be given by

$$I_k = \frac{a_k}{a_0} I_0 \tag{2.7}$$

Let Δa be the displacement of the light beam in the vertical direction y above the knife-edge corresponding to the angular deflection (α'') of the beam passing through

the test region. From Fig. 2.5, Δa can be expressed as

$$\Delta a = \pm f_2 \alpha'' \tag{2.8}$$

The sign in Eq. 2.8 is determined by the direction of the displacement of the laser beam in the vertical direction; it is positive when the shift is in the upward direction and negative if the laser beam gets deflected below the knife-edge. In the following discussion, Eq. 2.8 is considered with a positive sign.

Let I_f be the final illumination on the screen after the light beam has deflected upwards by an amount Δa due to the inhomogeneous distribution of refractive index in the test cell. Hence

$$I_f = I_k \frac{a_k + \Delta a}{a_k} = I_k \left(1 + \frac{\Delta a}{a_k}\right) \tag{2.9}$$

The change in light intensity on the screen ΔI is given by

$$\Delta I = I_f - I_k$$

The contrast thus generated by the schlieren measurement is expressed as

$$\text{contrast} = \frac{\Delta I}{I_k} = \frac{I_f - I_k}{I_k} = \frac{\Delta a}{a_k} \tag{2.10}$$

Using Eq. 2.8

$$\text{contrast} = \frac{\Delta I}{I_k} = \frac{\alpha'' f_2}{a_k} \tag{2.11}$$

Equation 2.11 shows that the contrast in a schlieren system is directly proportional to the focal length of the second concave mirror i.e. f_2. Larger the focal length, greater will be the sensitivity of the system.

Combining Eqs. 2.6 and 2.11, the governing equation in a schlieren system is obtained as

$$\frac{\Delta I}{I_k} = \frac{f_2}{a_k} \int_0^L \frac{\partial n}{\partial y} \mathrm{d}z \tag{2.12}$$

Equation 2.12 shows that the schlieren technique records the *path integrated* gradient of refractive index over the length of the test section. If the field is 2D (in the $x - y$) plane, the quantity $\partial n / \partial y$ is independent of the z coordinate and

$$\frac{\Delta I}{I_k} = \frac{f_2}{a_k} \frac{\partial n}{\partial y} L \tag{2.13}$$

The quantity on the left-hand side can be obtained by using the initial and final intensity distributions on the screen. In the experiments discussed in the present monograph, the knife-edge is adjusted in such a way that it cuts off approximately 50 % of the original light intensity, i.e. $a_k = a_0/2$ where a_0 is the original dimension of the laser beam at the knife-edge. The exact value of a_0 cannot be measured. Its value is of the order of microns and can be confirmed only by validation against benchmark experiments. With $a_k = a_0/2$, we get

$$\frac{\Delta I}{I_k} = \frac{2 f_2}{a_0} \frac{\partial n}{\partial y} L \tag{2.14}$$

Equation 2.14 represents the governing equation for the schlieren process in terms of the ray-averaged refractive index field. Since ΔI is calculated purely in terms of the angle α, the model presented above requires that changes in light intensity occur due to beam deflection alone, rather than its physical displacement.

The above derivation can be repeated for a knife-edge held vertical so that x-derivatives of refractive index can be imaged on the screen. This approach makes the *paraxial* approximation in that the derivatives in x and y directions are taken to have independent influences on beam deflection. It is expected to hold under the small angle approximation adopted in this chapter.

If the working fluid is a gas, the first derivative of the refractive index field with respect to y can be expressed in terms of density using Eq. 2.2 as

$$\frac{\partial \rho}{\partial y} = \frac{\rho_0}{n_0 - 1} \frac{\partial n}{\partial y} \tag{2.15}$$

Equation (2.15) relates the gradient in the refractive index field with the gradients of the density field in the fluid medium inside the test cell. The governing equation for schlieren measurement in gas can be rewritten as

$$\frac{\Delta I}{I_k} = \frac{f_2}{a_k} \frac{n_0 - 1}{\rho_0} \frac{\partial \rho}{\partial y} L \tag{2.16}$$

Assuming that the pressure inside the test cell is practically constant, we get

$$\frac{\Delta I}{I_k} = -\frac{f_2}{a_k} \frac{n_0 - 1}{\rho_0} \frac{p}{R T^2} \frac{\partial T}{\partial y} L \tag{2.17}$$

Equations 2.16 and 2.17 respectively relate the contrast measured using a laser schlieren technique with the density and temperature gradients in the test section. With the dependent variables such as T defined away from a solid surface or with proper boundary conditions, these equations can be integrated to determine the quantity of interest. For a KDP solution arising in crystal growth applications [4–6], Eq. 2.3 governs the relationship between species concentration (expressed as a mole fraction N) and refractive index. The concentration gradient is now obtained as

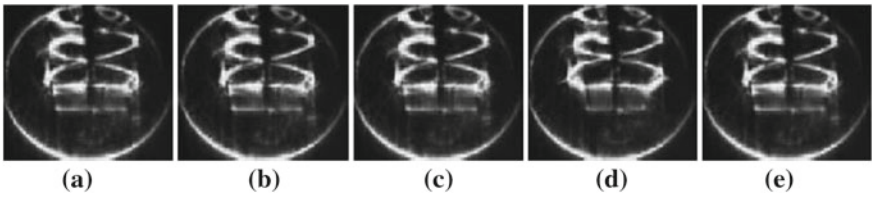

Fig. 2.6 Original schlieren images **a**–**d** of convective field as recorded by the CCD camera and the corresponding time-averaged image **e**, from [9]

$$\frac{\partial N}{\partial y} = \frac{9n}{2\alpha_{\mathrm{KDP}}(n^2+2)^2}\frac{\partial n}{\partial y} \tag{2.18}$$

where α_{KDP} is the polarizability of the KDP material in water (=4.0 cm^3/mole) and N is the molar concentration of the solution. Combining Eqs. 2.12 and 2.18 and integrating from a location in the bulk of the solution (where the gradients are negligible), the concentration distribution around the growing crystal can be uniquely determined.

Equations 2.16 and 2.17 show that the schlieren measurements are primarily based on the intensity distribution as recorded by the CCD camera. Since calculations are based on an intensity ratio, it is not necessary to record absolute intensity values. This step requires the camera to be a linear device that converts intensity to voltages stored in the computer. The linearity requirement can be fulfilled by ensuring that the camera does not get saturated with light intensity. A second implication of Eq. 2.14 is that original light intensities are required and schlieren images should not be subject to image processing operations. In practice, the camera sensors may show pixel-level scatter and it is common to average intensities over a 3×3 pixel template. In fluids, a perfectly steady convective field may not be attained and temporal fluctuations are possible. In such instances, a certain amount of time-averaging is performed before starting data analysis. Figure 2.6 shows one such set of four schlieren images recorded as a time sequence and their averaged image. The images show the convective plume in the form of high intensity regions above a crystal growing from its aqueous solution and are discussed in detail in [9].

2.2.2.1 Window Correction

For imaging the temperature or concentration field by laser schlieren, optical windows are often used to contain the fluid region within. Such windows must be used while working with liquids, but may be required in gases as well if the influence of the environment is to be minimized. The optical windows employed are of finite thickness (say, 5 mm) and the index of refraction of its material (for example, BK-7) is considerably different from that of the liquid within and the ambient air. The light beam emerging out of the test section with an angular deflection undergoes refraction

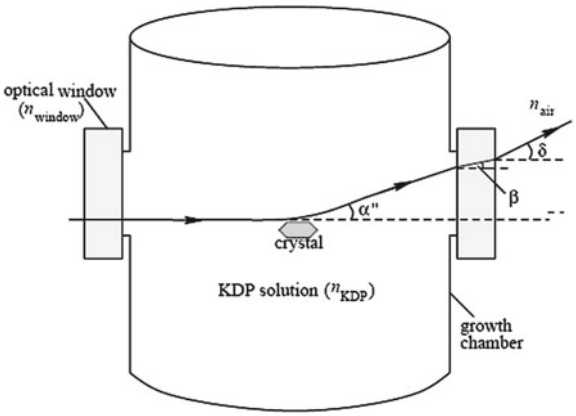

Fig. 2.7 Schematic drawing of the path of the light beam and the corresponding angles of deflection as it passes through the growth chamber. Angles shown are exaggerated for clarity

again before falling on the second concave mirror. The contribution of refraction at the confining optical windows can be accounted for by applying a correction factor to Eq. 2.14 as discussed below.

Consider the growth of a KDP crystal from its supersaturated solution in water as shown in Fig. 2.7. The laser beam strikes the second optical window fixed on the growth chamber at an angle after undergoing refraction due to variable concentration gradients in the vicinity of the growing KDP crystal. The optical windows have an index of refraction equal to n_{window} (around 1.509). The refractive index of the KDP solution (n_{KDP}) at an average temperature of 30 °C is 1.355, and for air n_{air} is close to unity. Let α'' be the angular deflection of the beam purely due to the presence of concentration gradients in the vicinity of the growing crystal, Fig. 2.7. The beam strikes the second optical window at this angle. Let β be the angle at which light leaves the inner surface of the second optical window. Using Snells law, we get

$$\frac{n_{\text{KDP}}}{n_{\text{window}}} = \frac{\sin\beta}{\sin\alpha''} \tag{2.19}$$

Since α'' is quite small in most applications, $\sin\alpha'' \approx \alpha''$ and

$$\sin\beta \approx \beta = \left(\frac{n_{\text{KDP}}}{n_{\text{window}}}\right)\alpha'' \tag{2.20}$$

Let δ be the final angle of refraction with which the laser beam emerges into the surrounding air. For the optical window-air combination

$$\left(\frac{n_{\text{window}}}{n_{\text{air}}}\right) = \frac{\sin\delta}{\sin\beta} \tag{2.21}$$

Hence

$$\sin\delta = \left(\frac{n_{\text{window}}}{n_{\text{air}}}\right) = \left(\frac{n_{\text{KDP}}}{n_{\text{window}}}\right)\alpha'' \tag{2.22}$$

or

$$\sin\delta \approx \delta = \left(\frac{n_{\text{KDP}}}{n_{\text{air}}}\right)\alpha'' \tag{2.23}$$

In experiments with optical windows, schlieren image analysis discussed in the previous sections would have to be carried out by first computing α'' from the recorded angle δ.

2.2.3 Gray-Scale Filter

The knife-edge of a conventional schlieren system is an excellent device for improving light intensity contrast in the optical image, but suffers from certain drawbacks. For example, gradients parallel to the knife-edge do not contribute to image formation. When the light beam is deflected below the knife-e.g., the gradient information is lost. Higher order effects such as a focus formed beyond the knife-edge may arise in measurements. Intensity modulation can also occur from diffraction of light at the sharp e.g., resulting in stray interference patterns superimposed on the schlieren image. Many of these drawbacks can be addressed by using a gray-scale (*graded*) filter. The filter is a photographic film on which a computer generated gray-scale is printed. The filter width may match that of the knife-edge. The vertical extent of the filter can be tuned to the deflections of light anticipated on the filter plane. The grayscale values of light intensity may vary from 0 to 255 (for a camera with 8-bit resolution) or a part of the range. The initial setting of the filter with respect to the undisturbed light spot is also an adjustable quantity. If the spot falls at the center of the filter, positive as well as negative beam deflections can be determined. The knife-edge can be thought of as a special construction of a gray-scale filter with two shades of 0 and 255 with a sharp cutoff.

In schlieren measurements with lenses, the diverging light beam from the spot formed over the knife-edge falls on a screen and the image recorded by the camera. In a *Z*-type configuration, the camera may be focussed on the light spot falling on the knife-edge. However, such an arrangement can lead to camera saturation. It is preferable to allow image formation on a screen and record the image at parallel incidence. In a graded filter arrangement, the filter itself acts as the screen and the camera records the image directly from it. In this approach, the filter needs to be calibrated for light intensity as a function of beam displacement at the filter location. This step is conveniently carried out when the test cell is undisturbed and the filter, mounted on a vertical traverse, moves relative to the spot of light. Under test conditions, the change in intensity at a point is mapped to beam displacement via the calibration curve. When a white light source such as a xenon lamp is used, an additional lens

may be used to collimate light from the spot formed at the filter plane and deliver it to the CCD camera.

Variations in the absorptivity of the photographic film (or the material used as a graded filter) can influence intensity measurement. An alternative is to use a color filter along with a color CCD camera. Here, color measured in terms of hue, dispenses with intensity, and material imperfections do not give rise to additional errors in measurements. A color filter used instead of the gray-scale, generates color images of the convective field. This approach, called *rainbow schlieren* is discussed in Chap. 3.

2.3 Background Oriented Schlieren

Background oriented schlieren (BOS) is a technique in which image variations of a distinct background are analyzed to determine density variations in a flow field. The index of refraction of a transparent medium has a direct correspondence to the density of the fluid. Therefore, density gradients cause index of refraction gradients. Rays of light passing through a test section are bent, to an extent that depends on the density gradient in the experimental test cell. This process alters the perception of the background image. The dependence of image formation on the refractive index field in BOS is similar to the basic schlieren setup, but BOS can be implemented in a much simpler apparatus as discussed below.

2.3.1 Experimental Details

The schematic drawing of a BOS setup is shown in Fig. 2.8. While the basic schlieren configuration often needs several high-quality lenses and mirrors guide the light beam, BOS needs only an illuminated background image, a CCD camera, and a computer with image acquisition software. The absence of precision optical components makes BOS a cheaper alternative. It also allows BOS to be more easily scalable to whatever size and precision is needed to accurately capture the density field in and around a given test model. A classical schlieren is preferably operated in a darkroom environment, since any ambient light can contaminate the image. In contrast, a BOS can operate with additional light sources, as the BOS technique is based on the virtual displacement of the background image, not just the intensity of light reaching the camera. In order for BOS to generate meaningful images, the background image must have high contrast and must be sensitive to small displacements. A randomized grid of small black dots on a white background serves this purpose well.

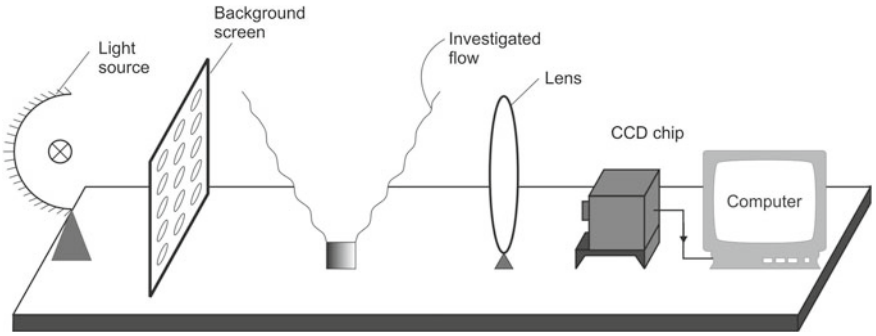

Fig. 2.8 Schematic diagram of the background oriented schlieren setup

2.3.2 Data Analysis

Figure 2.9 is a schematic drawing that explains the principle behind imaging by a BOS system. Here, z represents the coordinate along the light path, f is the focal length of the camera lens, Z_c is the distance from the camera to the phase object field, and Z_B is the distance from the phase object to the background image. The local image displacement χ can be expressed by integrating the local refractive index gradients along the light path as:

$$\chi = \frac{f Z_B}{Z_C + Z_B - f} \int_{\Delta_z} \frac{1}{n_0} \frac{\partial n}{\partial r} \mathrm{d}z, \tag{2.24}$$

Here, n, refractive index field is a function of the cross-sectional plane coordinates (x, y). The 2D image displacement value $\chi(x, y)$ can be used to determine the partial derivatives $\partial\rho/\partial x$ and $\partial\rho/\partial y$ by using Lorentz–Lorenz relationship, as in image analysis used for the basic schlieren arrangement. BOS employs a computer generated dot pattern screen, placed behind the test cell. The object field (namely, the test cell) defined by its density variation is placed between the camera and the dot pattern. For BOS, two image sets are recorded. One dot pattern image is acquired without density effects. The second dot pattern image is acquired with the density gradient prevailing in the test cell. The displacements of the dots are calculated using an image displacement correlation algorithm. The software often used for this type of processing is readily adapted from particle image velocimetry (PIV), which is commonly used experimental fluid mechanics laboratories. The initial image may carry uniformly distributed dots or otherwise, and may be tailored to the application being studied. The second image can be a time sequence of images, if the phenomenon of interest is unsteady. While the displacement of particles in a series of PIV images corresponds to velocities, the displacement of background dots in BOS images correspond to the density variation. The spatial resolution of measurement is determined by the dot size. As opposed to basic schlieren, BOS measures, not small

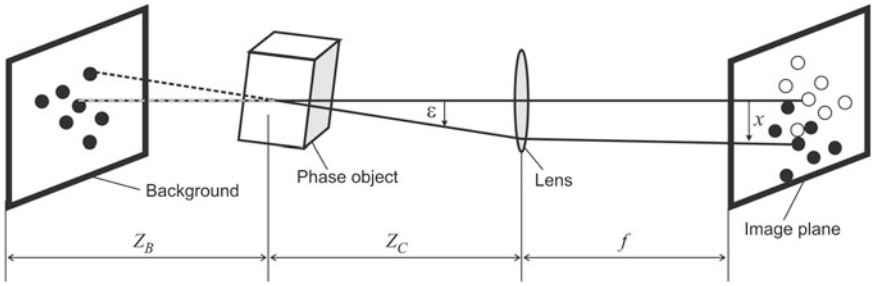

Fig. 2.9 Schematic drawing that explains the image formation in background oriented schlieren

angles but small displacements, and can be advantageous in certain contexts. Beam displacement errors (related to the shadowgraph effect) need to be accounted for during image analysis. An additional set of references on BOS is provided at the end of the chapter.

The cross-correlation algorithm used for determining displacement is shown schematically in Fig. 2.10. Let I_1 and I_2 be the interrogation regions of the initial and the final images being cross-correlated. The images are defined in terms of intensities at pixel indices (i, j) with the pixel sizes being Δx and Δy in the two directions. These indices run over $i = 1 \ldots M$ and $j = 1 \ldots M$. The cross-correlation function R_{12} between this pair of images is numerically evaluated as

$$R_{1,2}(i, j) = \sum_{l=1}^{M} \sum_{m=1}^{N} I_1(l, m) I_2(l + i - 1, m + j - 1), \quad i = 1 \ldots M; \quad j = 1 \ldots N$$

In practice, the cross-correlation function is evaluated using Fourier transforms to exploit the efficiency of the fast Fourier transform (FFT) algorithm. Let the 2D Fourier transforms of these images be respectively given as $\hat{I}_1$ and $\hat{I}_2$, while $*$ indicates complex conjugate. The symbol IFT is used for the inverse Fourier transform of its argument. In terms of Fourier transforms, the cross-correlation function is written as

$$R_{12} = \mathrm{IFT}\{\hat{I}_1 \times \hat{I}_2^{\,*}\}$$

Here, IFT is inverse Fourier transform and can also be evaluated using the FFT algorithm. Such calculations can be carried out using commercially available image analysis software. Displacement information associated with the interrogation spot is contained in the spatial coordinates (in integer multiples of the pixel size Δx and Δy) where the cross-correlation function attains its maximum. Displacement can now be related to beam deflection and hence, refractive index gradients prevalent in the physical domain.

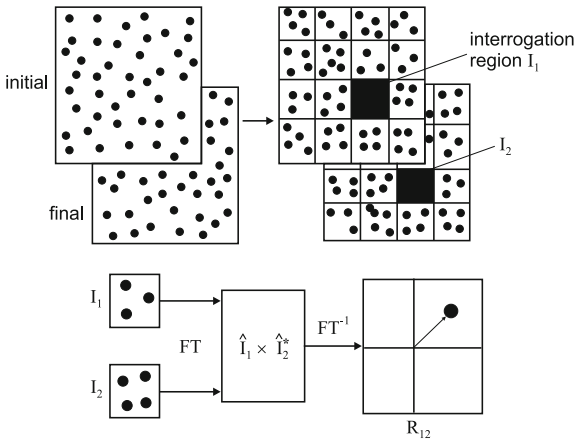

Fig. 2.10 Pictorial representation of the cross-correlation algorithm for displacement calculation

2.4 Shadowgraph Technique

Shadowgraph has been extensively used in experimental fluid mechanics and heat transfer but as a tool for flow visualization. Shadowgraph employs an expanded collimated beam of light from a laser that traverses the field of disturbance. If the disturbance is one of varying refractive index, the individual light rays passing through the test section are refracted and bent out of their original path. This causes a spatial modulation of the light-intensity distribution with respect to the original intensity on the screen. The resulting pattern is a shadow of the refractive index field prevailing in the region of the disturbance. Figure 2.11 shows the schematic drawing of the shadowgraph arrangement [11]. A He–Ne laser (15–35 mW power, continuous wave) is expanded and collimated to a suitable diameter by a beam expander. The collimated beam passes through the test section being investigated. The beam emerging from the exit window falls on a screen resulting in the shadowgraph image. The images may be recorded as individual frames or a video sequence by a suitable camera. A sample shadowgraph of a slightly heated water jet is shown in Fig. 2.12. Here, the initial instability as well as the breakdown of ring vortices to small-scale turbulence are visible.

The discussion related to intensity distortions by a screen in the context of schlieren carries over to the shadowgraph. With a laser as a light source, the screen can diminish light intensity and prevent camera saturation. When a distributed light source is used, the screen can be replaced by a lens arrangement that conveys all the available light to the CCD array. The advantage here is that the camera can focus on any plane beyond the test cell and the sensitivity of measurement suitable altered.

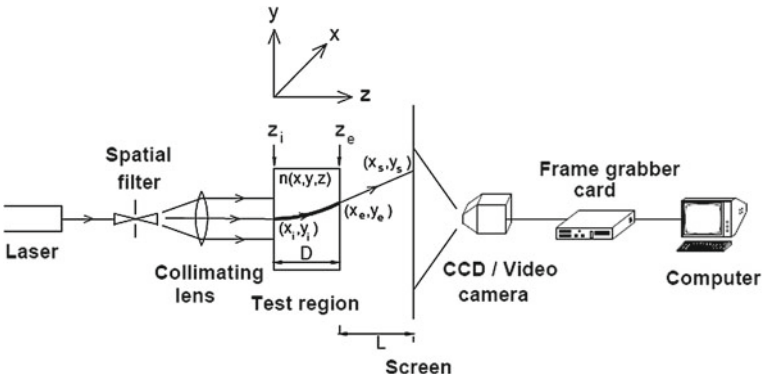

Fig. 2.11 Schematic drawing of the shadowgraph technique

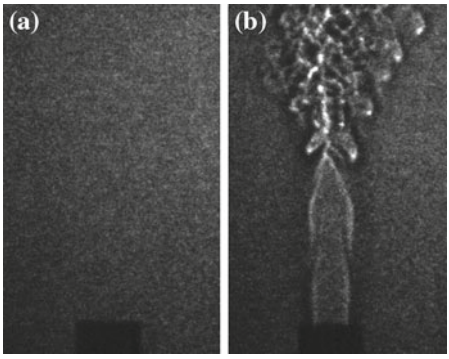

Fig. 2.12 **a** Initial image of the laser beam before flow is turned on. **b** Shadowgraph of a slightly heated water jet at a Reynolds number of 693 based on nozzle diameter and averaged fluid speed. Ring vortices initially formed and their progressive breakdown to turbulent structures are visible

2.4.1 Governing Equation and Approximations

Quantitative data can be extracted from shadowgraph images using the formulation discussed below [7, 11].

Consider a medium with refractive index n that depends on all the three space coordinates, namely $n = n(x, y, z)$. We are interested in tracing the path of light rays as they pass through this region. Starting with the knowledge of the angle and the point of incidence of the ray at the entrance plane, we would like to know the location of the point on the exit window, and the slope of the emergent ray [1, 7]. Let the ray be incident at point $p_i(x_i, y_i, z_i)$ while the exit point is $p_e(x_e, y_e, z_e)$. According to Fermat's principle, the optical path length (OPL) traversed by the light beam between these two points has to be an extremum. For a geometric segment ds along the path, the corresponding OPL is $n(x, y, z)$ds. The total OPL between the two points p_i and p_e is

$$\text{OPL} = \int_{p_i}^{p_e} n(x, y, z)\text{d}s$$

As per Fermat's principle

$$\delta\left(\int_{p_i}^{p_e} n(x, y, z)\mathrm{d}s\right) = 0 \tag{2.25}$$

Parameterizing the light path by z, the ray is fully defined by functions $x(z)$ and $y(z)$. Equation 2.25 can be rewritten as

$$\delta\left(\int_{z_i}^{z_e} n(x, y, z)\sqrt{x'^2 + y'^2 + 1}\mathrm{d}z\right) = 0 \tag{2.26}$$

where the primes denote differentiation with respect to z. Application of the variational principle to Eq. 2.26 generates the following two, coupled, Euler–Lagrange equations:

$$x''(z) = \frac{1}{n}(1 + x'^2 + y'^2)\left(\frac{\partial n}{\partial x} - x'\frac{\partial n}{\partial z}\right) \tag{2.27}$$

$$y''(z) = \frac{1}{n}(1 + x'^2 + y'^2)\left(\frac{\partial n}{\partial y} - y'\frac{\partial n}{\partial z}\right) \tag{2.28}$$

Here (for x)

$$x'(z) = \frac{\mathrm{d}x}{\mathrm{d}z} \text{ and } x''(z) = \frac{\mathrm{d}^2x}{\mathrm{d}z^2}$$

Equations 2.27 and 2.28 are second-order nonlinear ordinary differential equations for $x(z)$ and $y(z)$. The four constants of integration required to solve these equations come from the boundary conditions at the entry plane of the chamber. These are the co-ordinates $x_i = x(z_i)$ and $y_i = y(z_i)$ of the entry point as well as the local derivatives $x_i' = x'(z_i)$ and $y_i' = y'(z_i)$. The solution of the two differential equations yields two orthogonal components of the deflection of the light ray at the exit plane along with its slope and curvature. In most experiments, the light beam entering the apparatus is parallel (at normal incidence) and the respective slopes are zero, namely $x_i' = 0$ and $y_i' = 0$. Let the length of the experimental chamber containing the fluid be D and the screen located at a distance L beyond the exit plane. The z-coordinates of individual light rays at entry, exit, and on the screen are given by z_i, z_e and z_s respectively. Since the incident beam is normal to the entrance plane, there is no refraction at the first optical window. While the derivatives of all the incoming light rays at the entry plane are zero, the displacements $x_s - x_i$ and $y_s - y_i$ of a light ray on the screen (x_s, y_s) with respect to its entry position (x_i, y_i) are

$$x_s - x_i = (x_e - x_i) + L \times x'(z_e) \tag{2.29}$$

$$y_s - y_i = (y_e - y_i) + L \times y'(z_e) \tag{2.30}$$

Here, the coordinates x_e, y_e, and $x'(z_e)$, $y'(z_e)$ are given by the solutions of Eqs. 2.27 and 2.28. The first term accounts for refraction within the physical domain, while the second term is the passage of light in normal ambient, taken to be undisturbed, along a straight line. These equations define image formation on the screen in a shadowgraph process and provide a route toward indirect determination of refractive index distribution from the Euler–Lagrange equations.

The formulation given above can be simplified under the following assumptions:

Assumption 2.1 Assume that the light rays at normal incidence on the entrance plane undergo only infinitesimal deviations inside the inhomogeneous field, but have a finite curvature on leaving the experimental apparatus. The derivatives $x'(z_i)$ and $y'(z_i)$ are zero, whereas $x'(z_e)$ and $y'(z_e)$ at the exit plane are finite values. The assumption is justified in contexts where the medium is weakly refracting. Equations 2.27– 2.30 can now be simplified as

$$x''(z) = \frac{1}{n}\left(\frac{\partial n}{\partial x}\right) \tag{2.31}$$

$$y''(z) = \frac{1}{n}\left(\frac{\partial n}{\partial y}\right) \tag{2.32}$$

$$x_s - x_i = Lx'(z_e) \tag{2.33}$$

$$y_s - y_i = Ly'(z_e) \tag{2.34}$$

Rewriting Eqs. 2.33 and 2.34 as

$$x_s - x_i = L\int_{z_i}^{z_e} x''(z)\mathrm{d}z \tag{2.35}$$

$$y_s - y_i = L\int_{z_i}^{z_e} y''(z)\mathrm{d}z \tag{2.36}$$

and using Eqs. 2.31 and 2.32, Eqs. 2.35 and 2.36 become

$$x_s - x_i = L\int_{z_i}^{z_e} \frac{\partial(\log n)}{\partial x}\mathrm{d}z \tag{2.37}$$

$$y_s - y_i = L\int_{z_i}^{z_e} \frac{\partial(\log n)}{\partial y}\mathrm{d}z \tag{2.38}$$

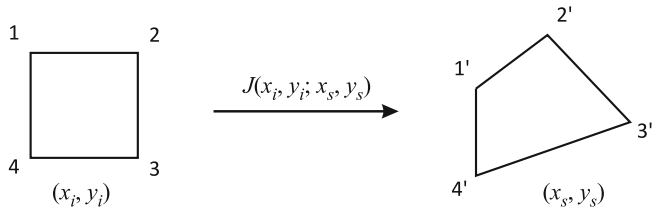

Fig. 2.13 Jacobian $J(x_i, y_i; x_s, y_s)$ of the mapping function connecting the original area (x_i, y_i) to the deformed area (x_s, y_s)

Note that the ray displacements are obtained as an *integration* over the length of the apparatus, and are *path integrals* in this respect.

Assumption 2.2 The assumption of infinitesimal displacement inside the growth chamber can be extended and taken to be valid even for the region falling between the screen and the exit plane of the chamber. As a result, the coordinates of the ray on the screen can be written as

$$x_s = x_i + \delta_x(x_i, y_i) \tag{2.39}$$

$$y_s = y_i + \delta_y(x_i, y_i) \tag{2.40}$$

The deviation of light rays from their original path in the physical medium results in a change of intensity distribution on the screen as compared to the original, when the physical region is undisturbed. Shadowgraph measures this change in the intensity distribution and relates it to the refractive index distribution. The intensity at point (x_s, y_s) on the screen is a result of several beams moving from locations (x_i, y_i) and getting mapped onto the point x_x, y_s on the screen. Since the initial spread of the light beam is deformed during its passage through the apparatus, the light intensity at point (x_s, y_s) is

$$I_s(x_s, y_s) = \sum_{(x_i, y_i)} \frac{I_0(x_i, y_i)}{\left| \frac{\partial(x_s, y_s)}{\partial(x_i, y_i)} \right|} \tag{2.41}$$

Here I_s is the intensity on the screen in the presence of an inhomogeneous refractive index field, and I_o is the original undisturbed intensity distribution. The denominator in the above equation is the Jacobian $J(x_i, y_i; x_s, y_s)$ of the mapping function that connects (x_i, y_i) with (x_s, y_s), as shown in the Fig. 2.13. Geometrically it represents the ratio of the area enclosed by four adjacent rays after and before passing through the test section. In the absence of any disturbance, a small rectangle maps onto a an identical rectangle of equal area and the Jacobian is unity. The summation in the above equation extends over all the rays passing through points (x_i, y_i) at the entry of the test section that are mapped onto the small quadrilateral (x_s, y_s) on the screen and contribute to the light intensity within.

Assumption 2.3 Under the assumption of infinitesimal displacements, the deflections δ_x and δ_y are small. Therefore, the Jacobian can be assumed to be linearly dependent on them. Neglecting higher powers of δ_x and δ_y and also their product, Jacobian can be expressed as

$$\left|\frac{\partial(x_s, y_s)}{\partial(x_i, y_i)}\right| \approx 1 + \frac{\partial(x_s - x_i)}{\partial x} + \frac{\partial(y_s - y_i)}{\partial y} \tag{2.42}$$

Substituting in Eq. 2.41, we get

$$I, (x_s, y_s)\left[1 + \frac{\partial(x_s - x_i)}{\partial x} + \frac{\partial(y_s - y_i)}{\partial y}\right] = \sum_{(x_i, y_i)} I_0(x_i, y_i) \tag{2.43}$$

Simplifying further

$$\frac{I_0(x_i, y_i) - I_s(x_s, y_s)}{I_s(x_s, y_s)} = \frac{\partial(x_s - x_i)}{\partial x} + \frac{\partial(y_s - y_i)}{\partial y} \tag{2.44}$$

Using Eqs. 2.37 and 2.38 for $(x_s - s_i)$ and $(y_s - y_i)$ and integrating over the dimensions of the experimental apparatus, we get

$$\frac{I_0(x_i, y_i) - I_s(x_s, y_s)}{I_s(x_s, y_s)} = (L \times D)\left(\frac{\partial^2}{\partial x^2} + \frac{\partial^2}{\partial y^2}\right)\log n(x, y) \tag{2.45}$$

Here, $n(x, y)$ is to be interpreted as an average value of refractive index over a length L in the z-direction. Equation 2.45 is the governing equation of the shadowgraph process under the set of linearizing approximations 1–3. In concise form the above equation can be rewritten as

$$\frac{I_0 - I_s}{I_s} = (L \times D)\nabla^2 \log n(x, y) \tag{2.46}$$

2.4.2 Numerical Solution of the Poisson Equation

The linearized governing differential equation of the shadowgraph process (Eq. 2.46) is a *Poisson* equation. In measurements, the left side of this equation is recorded as the shadowgraph image. The Poisson equation relates light intensity variation in the shadowgraph image to the refractive index field of the physical medium. In order to solve for refractive index, the following numerical procedure can be adopted. First, the Poisson equation is discretized over the physical domain of interest by a finite-difference method. The resulting system of algebraic equations is solved for the shadowgraph image under consideration to yield a depth-averaged refractive index value for each node of the grid. A mix of Dirichlet and Neumann conditions

are usually available to serve as boundary conditions. This approach is considerably simpler than solving the inverse problem indicated in Eqs. 2.27 and 2.28.

In order to assess the validity of assumptions 1–3, the importance of higher order optical effects in shadowgraph imaging need to be examined. This step is accomplished by determining the extent of bending of light rays in a field of known refractive index. A possible approach is to solve the Poisson equation for the refractive index field and then evaluate ray displacements from Eqs. 2.27 and 2.28 where refractive index appears as a parameter. A useful guideline for linearity to hold is that the Jacobian, constructed using four adjacent points and interpreted as per Fig. 2.13 remains within ± 5 % of unity.

2.5 Closure

Image formation in interferometry, schlieren, and shadowgraph relies on refractive index changes in the physical domain. Interferometry has a larger number of optical elements. Since it is based on differential measurement of phase, it is sensitive to alignment. Schlieren has fewer optical components and is less sensitive and shadowgraph, being the simplest configuration, is the least sensitive to factors, such as alignment, vibrations, and other extraneous factors. Interferograms are quite vivid, since fringes are isotherms (iso-concentration lines) and unambiguously represent the temperature (concentration) field. The discusson in Chap. 1 shows that the analysis of interferograms is quite straightforward. Schlieren and shadowgraph images reveal regions of high concentration gradients in the form of heightened (or diminished) brightness. Temperature and concentration can be recovered in schlieren by integrating the intensity distribution. In shadowgraph, a Poisson equation needs to be solved, subject to suitable boundary conditions. Thus, a shadowgraph experiment is the easiest to perform while the analysis of shadowgraph data is the most complicated. Schlieren, in this respect, falls between interferometry and shadowgraph with modest demands on experimental complexity and data reduction.

The three refractive index-based techniques yield images that are integrated values of temperature/concentration (or their derivative in a cross-sectional plane) in the direction of propagation of the light beam. If the spatial extent of the disturbed zone in the domain is small, the information contained in the image is small. In the context of interferometry, the consequence could be the appearance of too few fringes in the infinite fringe setting and small fringe deformation in the wedge fringe setting. In schlieren and shadowgraph, weak disturbances show up as small changes in intensity and hence, contrast. The difficulty can be alleviated in schlieren by using large focal length optics so that small deflections are amplified. In shadowgraph, image quality can be improved by moving the screen away from the test cell. The sensitivity of interferometric measurements can be improved by using techniques such as phase shifting but they require additional optical components and revised analysis tools. Additional difficulties with interferometry are the need for maintaining identical experimental conditions in the test section and the compensation chamber, careful

balancing of the test and the reference beams, and limitations arising from the fact that quantitative information is localized at the fringes.

This discussion shows that configuring the interferometer as an instrument for process control poses the greatest challenge, schlieren, and shadowgraph being relatively simpler. Schlieren may be considered as an optimum while comparing the ease of analysis with the difficulty of instrumentation.

References

1. Born M, Wolf E (1980) Principles of optics. Pergamon Press, Oxford
2. Gebhart B, Jaluria Y, Mahajan RL, Sammakia B (1988) Buoyancy-induced flows and transport. Hemisphere Publishing Corporation, New York
3. Goldstein RJ (ed) (1996) Fluid mechanics measurements. Taylor and Francis, New York
4. Mantani M, Sugiyama M, Ogawa T (1991) Electronic measurement of concentration gradient around a crystal growing from a solution by using Mach-Zehnder interferometer. J Cryst Growth 114:71–76
5. Onuma K, Tsukamoto K, Nakadate S (1993) Application of real time phase shift interferometer to the measurement of concentration field. J Cryst Growth 129:706–718
6. Rashkovich LN (1991) KDP family of crystals. Adam Hilger, New York
7. Schopf W, Patterson JC, Brooker AMH (1996) Evaluation of the shadowgraph method for the convective flow in a side-heated cavity. Exp Fluids 21:331–340
8. Settles GS (2001) Schlieren and shadowgraph techniques. Springer, Berlin, p 376
9. Srivastava A (2005) Optical imaging and control of convection around a KDP crystal growing from its aqueous solution, Ph.D. thesis, IIT Kanpur (India)
10. Tropea C, Yarin AL, Foss JF (eds) (2007) Springer handbook of experimental fluid mechanics. Springer, Berlin
11. Verma S (2007) Convection, concentration and surface feature analysis during crystal growth from solution using shadowgraphy, interferometry and tomography, Ph.D. thesis, IIT Kanpur (India)
12. Atcheson B, Heidrich W, Ihrke I (2009) An evaluation of optical flow algorithms for background oriented schlieren imaging. Exp. in Fluids 46:467–476
13. Goldhahn E, Seume J (2007) The background oriented schlieren technique: sensitivity, accuracy, resolution and application to a three-dimensional density field. Exp. in Fluids 43:241–249
14. Kindler K, Goldhahn E, Leopold F, Raffel M (2007) Recent developments in background oriented Schlieren methods for rotor blade tip vortex measurements. Exp. Fluids 43:233–240
15. Ramanah D, Raghunath S, Mee DJ, Rsgen T, Jacobs PA (2007) Background oriented schlieren for flow visualisation in hypersonic impulse facilities. Shock Waves 17:65–70
16. Roosenboom EWM, Schroder A (2009) Qualitative Investigation of a Propeller Slipstream with Background Oriented Schlieren. Journal of Visualization 12(2):165–172
17. Sommersel OK, Bjerketvedt D, Christensen SO, Krest O, Vaagsaether K (2008) Application of background oriented schlieren for quantitative measurements of shock waves from explosions. Shock Waves 18:291–297
18. Sourgen F, Leopold F, Klatt D (2012) Reconstruction of the density field using the Colored Background Oriented Schlieren Technique(CBOS). Optics and Lasers in Engg 50:29–38
19. Venkatakrishnan L, Meier GEA (2004) Density measurements using the Background Oriented Schlieren technique. Exp. in Fluids 37:237–247